Voltage-induced defect mode coupling in a one-dimensional photonic crystal with a twisted-nematic defect layer

Ivan V. Timofeev,[1,2,*] Yu-Ting Lin,[3] Vladimir A. Gunyakov,[1,2] Sergey A. Myslivets,[1] Vasily G. Arkhipkin,[1,2] Stepan Ya. Vetrov,[2] Wei Lee,[4,5] and Victor Ya. Zyryanov[1,6]

[1]*L. V. Kirensky Institute of Physics, Krasnoyarsk Scientific Center, Siberian Branch of the Russian Academy of Sciences, Krasnoyarsk 660036, Russia*

[2]*Siberian Federal University, Krasnoyarsk 660041, Russia*

[3]*Master Program in Nanotechnology, Chung Yuan Christian University, Chung-Li 32023, Taiwan*

[4]*Department of Physics, Chung Yuan Christian University, Chung-Li 32023, Taiwan*

[5]*Center for Nanotechnology, Chung Yuan Christian University, Chung-Li 32023, Taiwan*

[6]*Siberian State Aerospace University, Krasnoyarsk 660014, Russia*

(Received 21 October 2011; revised manuscript received 7 December 2011; published 17 January 2012)

Defect modes are investigated in a band gap of an electrically tunable one-dimensional photonic crystal infiltrated with a twisted-nematic liquid crystal. Their frequency shift and interference under applied voltage are studied both experimentally and theoretically. We deal with the case where the defect layer thickness is much larger than the wavelength (i.e., the Mauguin condition). It is shown theoretically that the defect modes could have a complex structure with elliptic polarization. Two series of polarized modes are coupled with each other and exhibit an avoided crossing phenomenon in the case of opposite parity.

DOI: 10.1103/PhysRevE.85.011705 PACS number(s): 42.70.Df, 61.30.Gd, 42.70.Qs, 07.05.Tp

I. INTRODUCTION

Photonic crystals (PCs) are optical materials that allow a rich optical response to be obtained by means of spatial inhomogeneity [1]. Defects in such structures with periodicity cause extreme characteristics in optical response. By introducing a tunable defect substance, the optical spectrum can be further controlled. Liquid crystals (LCs) are well-known, promising materials featuring sensitive anisotropy, dispersion, nonlinearity, and susceptibility to external stimuli, such as temperature, electric and magnetic fields, and light [2–8]. Combining the above concepts, PCs infiltrated with nematic LC as a defect (PCNLC) were suggested [9–12]. PCNLC allows manipulation with the defect transmission peaks to be carried out in the photonic band gap (PBG). Self-organized PCs with various types of pitch defects were studied in cholesteric LCs as well [13]. Furthermore, an anisotropic Fabry-Perot resonator cavity has two orthogonally polarized mode series [14]. The concept of two mode series (O- and E-modes) was applied to the PCNLC system to reveal that the wave interference depends on the mode parity [15–18].

Investigation of a twisted-nematic (TN) defect in PC (PCTN) was initiated in [14,19]. The average molecular orientation (director) of the rodlike NLC is twisted by 90° using orthogonal planar boundary conditions. This twist provides coupling between O- and E-modes, which leads to elliptic polarization of the defect mode. Our goal in this paper is to clarify the underlying processes behind the experimental data reported in Ref. [19].

II. NUMERICAL ANALYSES

Numerical routines can be used to find both the LC orientation and PCTN optical response. The first step is to calculate the reorientation of the LC director inside a TN cell (TNC) [Fig. 1(a)] under an applied voltage. The voltage is applied across the cell thickness (along the z axis; see Fig. 2). Before we start our calculation, it is instructive to predict the result qualitatively [20]. Let us roughly assume a LC cell to consist of two boundary layers and a middle layer. Voltages higher than the Fréedericksz threshold [21] force the LC director to lie along the z axis (known as homeotropic orientation), whereas the boundary LC layers remain in planar alignment due to the surface anchoring. The middle layer then acquires homeotropic orientation and loses azimuthal rigidity. In this case, the azimuthal coupling between the left and the right boundaries vanishes and both boundary layers return to their respective rubbed planes [Fig. 1(b)]. The homeotropic middle layer acts as a lubricator. The applied voltage gives rise to the homeotropic lubrication effect. The azimuthal angle φ of the LC director varies slowly near the boundaries yet exhibits a steeper behavior in the middle. Increasing voltages lead to the growth of the middle homeotropic layer and the simultaneous reduction of the planar boundary layers [Fig. 1(c)] until the thickness of the boundary layers approaches the electric coherence length ξ, which becomes much smaller than the wavelength of the incident light, λ.

Minimization (variation) of free enthalpy is a classical method to determine the LC director orientation. While the mechanical increment of free enthalpy is negligibly small, it is common to minimize the free energy [22,23]. An analytical solution for twisted LC in an electric field is rather involved [24]. A numerical solution of the boundary-value problem using the shooting method [25] is appropriate for in-plane LC orientation, whereas for twisted LC it is sufficient to use a simple general method of gradient descent to the free energy minimum [26]. The elastic energy of a homogeneous LC layer is expressed as [23]

$$2F_k = \bar{k}_b\tilde{\theta}^2 + \bar{k}_t\tilde{\varphi}^2\cos^2\theta. \quad (1)$$

*Corresponding address: L. V. Kirensky Institute of Physics, Krasnoyarsk Scientific Centre, SB RAS, Krasnoyarsk, 660036, Russia; tiv@iph.krasn.ru

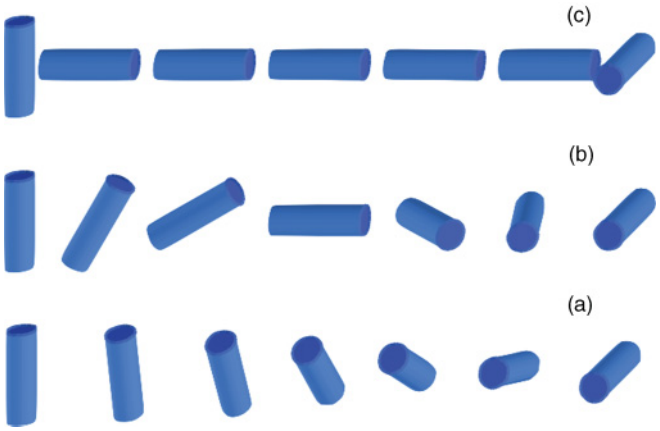

FIG. 1. (Color online) Schematic of LC reorientation in a TNC under applied voltage. (a) Constant rotation at voltages below the Fréedericksz threshold. (b) Homeotropic lubrication. (c) High voltage reduces boundary planar layers.

Here θ and φ are, respectively, the angle of the LC director deviation from the substrate plane and the azimuthal angle of the director $\vec{n}$, whose components are $n_x = \cos\theta\cos\varphi$, $n_y = \cos\theta\sin\varphi$, and $n_z = \sin\theta$. The tildes in Eq. (1) represent a partial derivative with respect to the cell depth, for example, $\tilde{\theta} = \partial\theta/\partial z = \partial_z\theta$, where ∂_z is the partial derivative operator with respect to the z axis. The effective elasticity coefficients, $\bar{k}_b$ and $\bar{k}_t$, are given by

$$\begin{aligned} \bar{k}_b &= k_{11}\cos^2\theta + k_{33}\sin^2\theta, \\ \bar{k}_t &= k_{22}\cos^2\theta + k_{11}\sin^2\theta, \end{aligned} \tag{2}$$

where k_{11}, k_{22}, and k_{33} are the splay, twist, and bend elasticity coefficients, respectively.

The continuum theory of NLC treats free energy density as a continuous function of coordinate (z axis). A numerical approach converts this function into a discrete array of

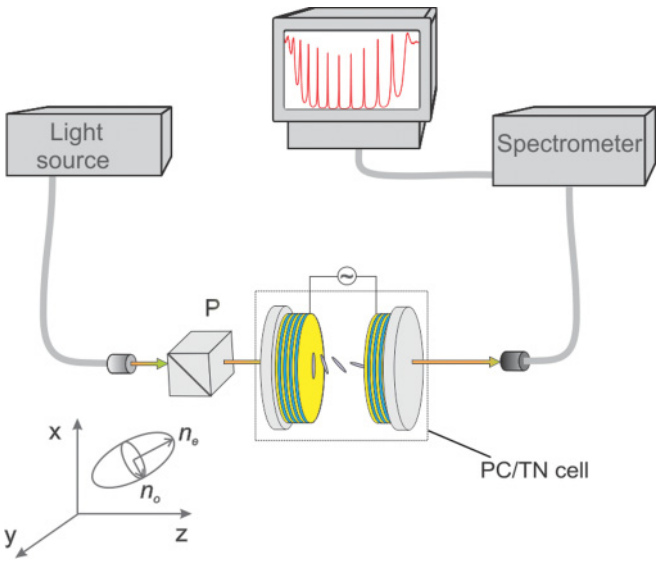

FIG. 2. (Color online) Experimental layout for the measurement of transmission spectra of a PCTN cell. The light source and spectrometer blocks are built-in components of the Shimadzu UV-3600 spectrophotometer. "P" is a polarizer.

numbers, corresponding to thin, semihomogeneous sublayers. In this study we use 100 sublayers for fairly accurate solution. Numerical convergence is controlled by artificial viscosity. The free energy variation is

$$\delta F_k = \delta_\theta F_k\,\delta\theta + \delta_\varphi F_k\,\delta\varphi. \tag{3}$$

Here $\delta_\theta = \delta/\delta\theta$ and $\delta_\varphi = \delta/\delta\varphi$ are the functional derivative operators. $\delta_\theta F_k$ and $\delta_\varphi F_k$ are the functional derivatives, known as Frechet derivatives:

$$\begin{aligned} 2\delta_\theta F_k = {} & (\delta_\theta \bar{k}_b)\tilde{\theta}^2 + \bar{k}_b(\delta_\theta\tilde{\theta}^2) \\ & + (\delta_\theta \bar{k}_t)\tilde{\varphi}^2\cos^2\theta + \bar{k}_t\tilde{\varphi}^2(\delta_\theta\cos^2\theta), \end{aligned} \tag{4}$$

$$2\delta_\varphi F_k = \bar{k}_t\left(\delta_\varphi\tilde{\varphi}^2\right)\cos^2\theta. \tag{5}$$

The numerical approach converts the functional derivative into a one-sublayer free energy gradient. Sublayer z_i with angles θ_i and φ_i gives

$$\begin{aligned} 2\delta_{\theta_i} F_k = {} & \left(\partial_{\theta_i}\bar{k}_b\right)\tilde{\theta}^2 + \bar{k}_b\left(\partial_{\theta_i}\tilde{\theta}^2\right) \\ & + \left(\partial_{\theta_i}\bar{k}_t\right)\tilde{\varphi}^2\cos^2\theta + \bar{k}_t\tilde{\varphi}^2\left(\partial_{\theta_i}\cos^2\theta\right) \end{aligned} \tag{6}$$

and

$$2\delta_{\varphi_i} F_k = \bar{k}_t\left(\partial_{\varphi_i}\tilde{\varphi}^2\right)\cos^2\theta. \tag{7}$$

The five gradient components can be interpreted as elastic torques of an opposite sign. At a fixed voltage the total electric contribution to the free energy density includes the electrostatic energy of the LC sublayer and the physical work of the voltage source and is expressed as [22]

$$\begin{aligned} F_e &= \frac{1}{2}\vec{D}\cdot\vec{E} - \vec{D}\cdot\vec{E} = -\frac{1}{2}\vec{D}\cdot\vec{E} \\ &= \frac{1}{2}\frac{-D_z^2}{(\varepsilon_\perp\cos^2\theta + \varepsilon_{||}\sin^2\theta)}. \end{aligned} \tag{8}$$

This one-dimensional problem restricts the electric induction to depend on the z axis only. Moreover, this dependence vanishes as long as the divergence of the electric displacement is zero or

$$|\vec{D}| = D_z = \text{const}(z). \tag{9}$$

The total electrostatic energy Φ of a cell can be expressed by voltage U as the following:

$$\Phi = \int_0^L F_e dz = \frac{-U^2}{2\int_0^L(\varepsilon_\perp\cos^2\theta + \varepsilon_{||}\sin^2\theta)^{-1}dz}. \tag{10}$$

Again, the electrostatic polarization torque of the ith sublayer is equal to the partial derivative of energy with respect to the angle θ_i at a constant voltage U on the electrodes. Here we ignore polarization of the alignment layers. Experimentally, the alignment layer cannot be moved outside the electrodes.

Another routine was used for simulation of PCTN optical response. The case of normal light incidence was considered. To verify the experimental results, we calculated transmission spectra under increasing voltage. The optical response was found using the Berreman method—the transfer-matrix method generalized for an anisotropic medium [27,28]. In the case of isotropic layered media, electromagnetic radiation can be divided into two independent (uncoupled) modes. These are two modes with orthogonal electric field vectors. Since they are

uncoupled, the matrix method involves manipulation of 2×2 matrices to describe propagation of the forward and backward Rayleigh waves. In the case of birefringent layered media, the electromagnetic radiation consists of four partial waves. Mode coupling takes place at the interface where an incident plane wave produces waves with different polarization states due to anisotropy of the layers. As a result, 4×4 matrices are required in the matrix method [29,30]. Both orientation and optical routines were implemented in MATLAB for calculations.

III. EXPERIMENTAL SETUP AND MEASUREMENT

A layout of the electro-optical one-dimensional PCTN cell used in our experiments is shown in Fig. 2. It contained two identical dielectric mirrors and a TN LC as a defect layer. The multilayer film of each mirror was comprised of six layers of a high-index substance, zirconium dioxide (ZrO_2) with refractive index $n_1 = 2.04$ and thickness $l_1 = 0.052$ μm, and five layers of low-index dielectric, silicon dioxide (SiO_2) with refractive index $n_2 = 1.45$ and thickness $l_2 = 0.102$ μm. These layers were deposited in an alternating sequence onto fused quartz substrates provided with a conductive coating of indium tin oxide (ITO). We chose the well-known LC, 4-*n*-pentil-4′-cyanobiphenyl (5CB) with nematic phase between 22.5 °C and 34 °C as the defect material. Planar alignment was obtained by a thin polyvinyl alcohol (PVA) layer. A twist of 90° was achieved by a silk rubbing procedure on the alignment layers. The defect layer was formed by 10 μm spacers and the parallelism was ensured by removing all Newton's rings in the process of cell assembly. The anisotropic refractive indices of 5CB were $n_\parallel = 1.719$ and $n_\perp = 1.536$ ($T = 23$ °C, $\lambda = 589$ nm) with respect to the parallel ($\parallel$) and perpendicular ($\perp$) components of the nematic director $\vec{n}$, respectively. A Glan prism polarizer was placed parallel (x axis) or perpendicular (y axis) to the incident-side rubbing direction. An ac applied voltage with sinusoidal waveform at 800 Hz was used to unwind the twisted structure into a homeotropic configuration. Transmission spectra for normally incident light were measured with a high-resolution spectrophotometer (Shimadzu UV-3600). A typical appearance of the transmission spectrum considered in this study is presented in Fig. 3(a).

Besides the choice of materials and the cell preparation technology, this experimental setup has some principal distinctions from [19]. First, the electrodes were formed on the ZrO_2 layer (between LC and the mirror) to provide a more accurate account of the applied voltage. Second, the defect and the alignment layers are much thicker. This feature increases the number of defect modes and makes their dynamic behaviors (spectral shift under applied voltage) richer and more complicated.

IV. COMPARISON OF EXPERIMENTAL AND NUMERICAL RESULTS

The experimental transmission spectrum of PCTN PBG is shown in Fig. 3(a) for a polarizer oriented transversely to the direction of rubbing on the input mirror. The defect transmission peaks in the center of PBG are damped by material absorption and light scattering. Four peaks are magnified in Fig. 3(b). In the simulation (dashed line) the following parameters were used: the ITO film ($n_{\mathrm{ITO}} = 1.88858 + 0.006i$, $d_{\mathrm{ITO}} = 140$ nm), fused quartz substrate ($n_{\mathrm{Sub}} = 1.45$), alignment layer ($n_{\mathrm{PVA}} = 1.515$, $d_{\mathrm{PVA}} = 1000$ nm), and LC defect layer ($n_{\mathrm{e}} = 1.701 + 3.9 \times 10^{-4}i$, $n_{\mathrm{o}} = 1.536 + 3.9 \times 10^{-4}i$, $d = 10\,815$ nm). The material dispersion has been taken into account. Note that both the PVA and LC defect layer thicknesses have been acceptably tuned to match the experimental results. In addition, the number and the position of defect transmission peaks correspond to the model structure when the defect layer is 815 nm thicker than the average spacer thickness. Material aging incurred n_{e} to be adjusted as well. As shown in Fig. 3(b), the agreement between the experimental and the simulated spectrum is exhilaratingly satisfactory. Although the material absorption has been taken into account, the intensity of defect modes in the calculated results is still slightly higher than the experimental one. The full width at half maximum of simulated defect modes is about 2 nm, which is comparable to the experimental data. The discrepancy between the measured and simulated spectra could be attributed to the slight light scattering caused by the structural interface roughness and other experimental uncertainties including imperfect fabrication of the multilayers.

Four transmission peaks in Fig. 3(b) were chosen to illustrate the typical spectral shift under applied voltage [Fig. 4(a)]. The shift of transverse components is a characteristic feature of twisted structure. This shift was first reported in [19] and had

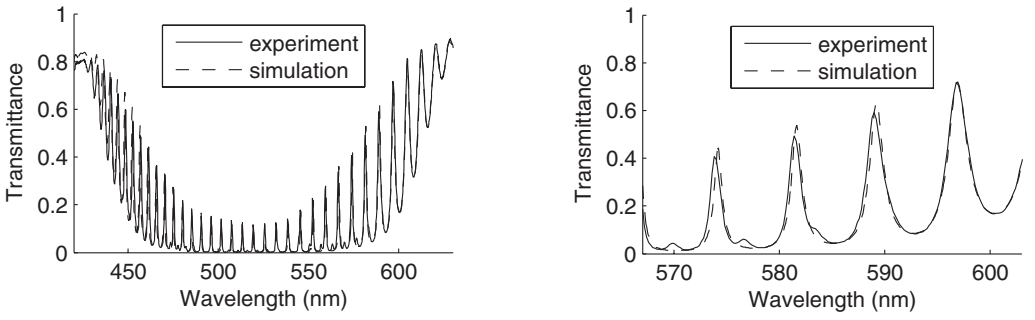

FIG. 3. Experimental (solid line) and numerical (dashed line) transmission spectra of the PCTN for transverse polarizer orientation. (a) Spectral data within the PBG. (b) An extended scale showing four typical defect transmission peaks.

FIG. 4. (a) Experimental and (b) simulated data of voltage-induced spectral shift of the four transmission peaks as shown in Fig. 3(b). The darker color corresponds to the higher transmittance. The numbers labeled on the top and the bottom in (b) stand for the mode numbers.

not been observed for in-plane LC orientation [15–18]. The numbers labeled in Fig. 4(b) are called the mode numbers, the concept of which has been mentioned in a previous work [18]. Each defect mode peak would have one mode number corresponding to the oscillating number of the electromagnetic waves in the medium, namely, the integer number of half wavelengths. In this sense, peaks can be identified by their mode numbers. For example, the leftmost peak at $\lambda = 573$ nm under no voltage has the same mode number, 68, as the peak at $\lambda = 575$ nm when $U = 10$ V_{rms}. At voltages near the Fréedericksz threshold, the number of peaks is doubled; when the voltages get higher, the minor peaks conceal into the major peaks. The spectral jump in mode numbers will be discussed in detail later. When the transmission axis of the polarizer is parallel to the rubbing direction, longitudinal molecular dipoles are excited. They produce extraordinary refraction which is extremely sensitive to the molecular director and reorientation. Therefore, the longitudinal spectrum is even more complicated and steeper (Fig. 5). Owing to the sensitivity of voltage-induced shift, the sampling interval is as small as $\Delta U = 0.02$ V, which allows the continuity of peak shift to be captured. When the voltage is beyond 1.4 V, a restructuring process occurs. The brighter peaks become less intense and slow down on the voltage-induced shift. The small peaks (or satellites) take over the major place and enlarge the shift. Simulation [Fig. 5(b)] predicts this restructuring at a lower voltage of 1.2 V due to the voltage drop on the alignment layers.

V. INTERPRETATION OF RESULTS

The series of small peaks called satellites was observed in the experimental spectrum for a transverse polarizer [Fig. 3(b)]. In fact, the wavelengths of these satellites correspond to those of major peaks of longitudinal polarization. This phenomenon can be explained by the experimental uncertainties that were not of concern in the model, such as possible structural domains with different sense of rotation, pretilt angle, and the alignment layer roughness visible at planar orientation. However, the said uncertainties are not the reasons for the existence of the satellites, which only enhance the irreducible satellites. Numerical simulation supports this fact qualitatively, but not quantitatively. The amplitude of numerical satellites is several times lower than in the experiment.

Actually, the satellites originate from the elliptic polarization of optical modes generated by the TNC structure. The adiabatic following in the TNC leads to the linearly polarized light being rotated along the twisted structure; in other words, the twisted adiabatic mode acts as a polarization waveguide. Considering a rodlike NLC with $n_o < n_e$, within a pair of parallel polarizers, the transmittance T can be expressed as a sinc function of adiabaticity [31,32]:

$$T = \left[\frac{\sin(\sqrt{1+u^2}\pi/2)}{\sqrt{1+u^2}}\right]^2, \tag{11}$$

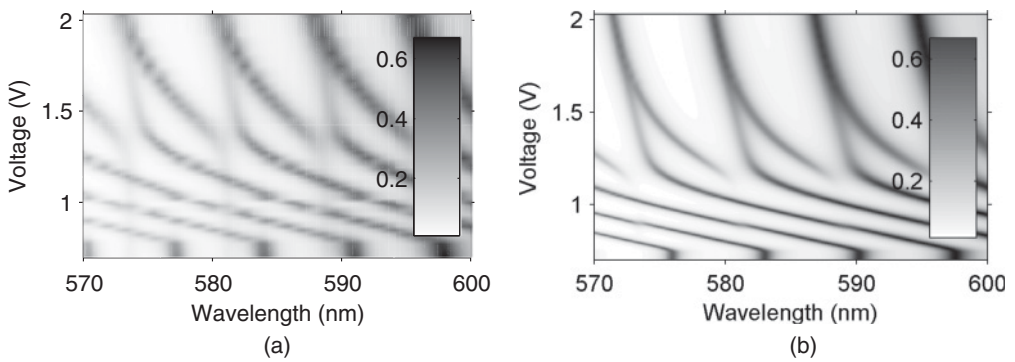

FIG. 5. Voltage-induced spectral shift of transmission peaks for longitudinal polarizer orientation mode. Darker color represents higher transmittance. (a) Experiment; (b) simulation.

where $u = 2d\Delta n/\lambda$ is the adiabatic Mauguin parameter (Δn is birefringence and d is the thickness of the LC layer). The Mauguin condition is $u \gg 1$.

Placing a twisted nematic between the PC mirrors brings about a new physics of the optical resonator. This resonator is conventionally named as the defect layer. Resonator modes of this resonator [33] are conventionally named as defect modes. The explanation of the spectral shift of transverse mode involves regenerative feedback and phase retardation. These phase retardations of optical modes are not equal to $2\pi d n_{o,e}/\lambda$. Effective refractive indices differ from ordinary and extraordinary indices of O- and E-modes. To avoid confusion, we introduce a slow semilongitudinal mode, L-mode, the first type of PCTN modes. L-mode is similar to E-mode in that its ellipse's long axis is parallel to the LC director. The sense of elliptic rotation of L-mode is opposite to the twist sense of the LC director. The other type of PCTN modes is fast semitransverse T-mode. The O-mode of nontwisted resonator is similar to T-mode, although O-mode has constant ordinary refractive index and cannot be shifted in frequency [12,15–18]. The sense of elliptic rotation of T-mode is the same as the twist sense of the LC director.

The numerical voltage-dependent transmission spectrum of unpolarized light is presented in Fig. 6. Four essential ranges are shown with dashed separators.

(I) $0 < U < U_C = 0.78$ V. There is no dynamics below the Fréedericksz threshold.

(II) 0.78 V $< U <$ 1.1 V. The L-mode peak series moves quickly towards the shorter wavelengths, but the T-mode peak series remains virtually at fixed wavelengths due to the Mauguin condition ensuring effective ordinary refractive index [Fig. 1 (a)].

(III) 1.1 V $< U <$ 2.0 V. The Mauguin condition breaks down in the thin middle layer [Fig. 1(b)]. LC in this layer exhibits a steep azimuthal rotation and low effective birefringence $\Delta n_{\text{eff}} \ll n$. T modes are coupled with L modes of opposite parity (see below).

(IV) 2.0 V $< U$. The voltage now is approximately three times higher than the Fréedericksz threshold. The middle LC layer has a virtually homeotropic director orientation [Fig. 1(c)]. The LC layers on the borders are in-plane-oriented and there is no twist and no Mauguin rotation of polarization. The L- and T-modes become linearly polarized. Vertical and horizontal directions without clockwise or counterclockwise twist become symmetric. Peaks of L- and T-modes with the same mode number combine to form doublets. These doublets experience a voltage-induced blueshift as the integral refractive index goes down with LC boundary layers thinning down.

Let us focus on ranges II and III, from which one can observe the unusual behavior in mode intersections. Figure 7(a) shows the cross of T-mode No. 68 and L-mode No. 74. The difference of numbers is even, indicating the same parity. Transmission peaks corresponding to these modes make linear superposition and cross each other under increasing voltage. A rough estimate for the number of half wavelengths inside the LC layer is yielded by the equality $N = 2nd/\lambda$:

$$N_T = 2 \cdot 10815/(574/1.536) = 57.9 \approx 68 - 10,$$
$$N_L = 2 \cdot 10815/(576/1.701) = 63.9 \approx 74 - 10. \quad (12)$$

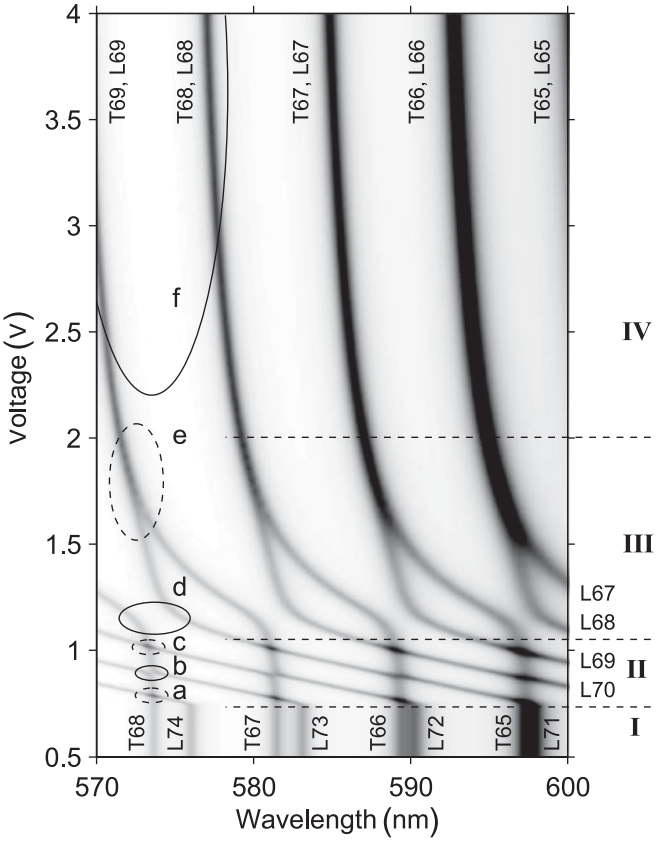

FIG. 6. Calculated transmission spectrum of unpolarized light versus voltage. Darker color corresponds to higher transmittance. The regions of intersection of T-mode No. 68 with L-modes No. 74 (a), 72 (c), 70 (e) are shown by dashed circles (same mode parity). The regions of coupling of T-mode No. 68 with L-modes No. 73 (b), 71 (d), 69 (f) are shown by solid circles (opposite mode parity). Dashed lines separate four voltage ranges exhibiting different types of mode behavior: below the threshold (I), L-mode shift (II), strong mode coupling (III), and doublets (IV).

Here we subtract the oscillations in the alignment layers, five oscillations in each layer. Obviously, standing-wave nodes do not occur exactly at the LC layer borders.

Figure 7(b) illustrates the coupling of T-mode No. 68 with L-mode No. 73, which have the opposite parity. Transmission peaks avoid crossing each other. The essential detail is the frequency shift of transmission peak nearby the other peak. This frequency shift has a general oscillatory nature and cannot be explained by interference only. The crossing is avoided due to mode coupling [33]. The same phenomenon was observed in [14] for small LC twist angle. The simply qualitative simulation of [14] is useful in spite of degeneration for perpendicular rubbing directions, considered in our case. Such crossing-avoidance phenomenon is well known in quantum mechanics as level repulsion phenomenon [34]. The crossing is avoided due to mode coupling. Normally, the crossing is observed at the intersection of opposite-parity modes [35]. In PCTN, however, it is contrary: the opposite-parity modes avoid crossing because the parity uses the mode spatial symmetry in the direction parallel rather than perpendicular to the transmission channel, and vice versa.

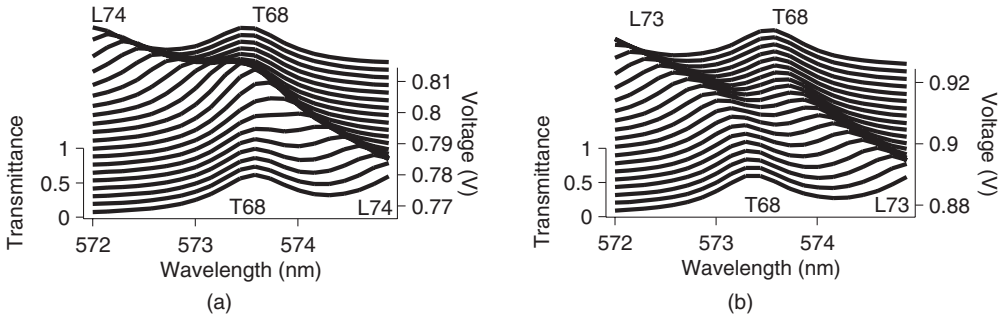

FIG. 7. The regions of mode intersection as zoomed in from encircled zones in Fig. 6. (a) Same-parity modes cross each other (see Fig. 6, zone a). (b) Opposite-parity modes avoid crossing (see FIG. 6, zone b).

The L-mode refractive index reduces with the increasing voltage, which leads to a blueshift of the L-mode wavelength. In Fig. 7(b), the long-wave peak (L73) shifts towards the shorter one (T68). Albeit the L- and T-mode wavelengths lie within a short distance, both of them are excited at the long-wave peak wavelength with the amplitudes a_{L} and a_{T}. Their superposition is an eigenmode with the electric field $\vec{E}_{lw}$ at long-wave peak:

$$\vec{E}_{lw} = a_{\mathrm{L}}\vec{E}_{\mathrm{L}} + a_{\mathrm{T}}\vec{E}_{\mathrm{T}}, \tag{13}$$

$\vec{E}_{\mathrm{L,T}}$ are field components corresponding to pure L- and T-modes. With the increasing voltage, a_{L} reduces from unity to zero, while a_{T} grows from zero to unity. The longitudinal-polarized transmitted light changes to a transverse-polarized light, and meanwhile slows down its shift rate. On the contrary, the short-wave peak changes from transversely polarized light to longitudinally polarized light and the peak shift rate increases. More precisely, the coupled modes "exchange" their peaks with each other. By analogy with quantum mechanics,

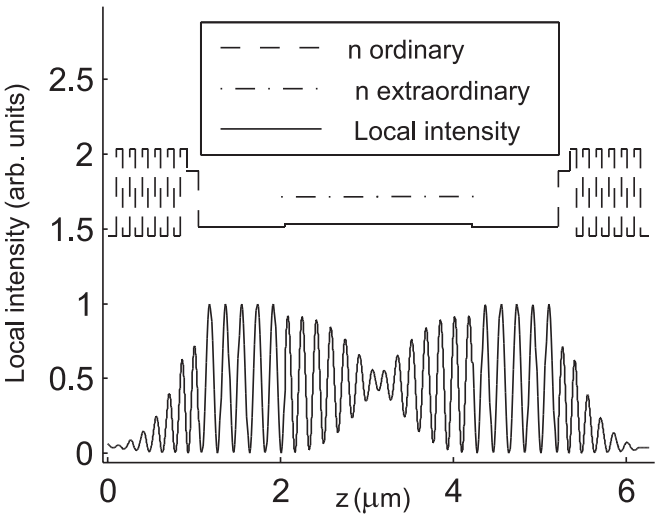

FIG. 8. Spatial distribution of local intensity inside the PCTN for L-mode at 558.1 nm. Oscillation suppression embarrasses calculation of the mode number. The parameters are the same as used to produce Fig. 3, except for the LC layer of 2.2 μm thickness, which is five times reduced to show the frequent oscillations in detail. The ordinary refractive index is shown by dashed line and the extraordinary refractive index in the NLC layer is indicated by a dash-dot line.

isolated modes are diabatic states and peaks refer to adiabatic superposition states. The number of half wavelengths inside the defect is not conserved for the transmission peak. This discrete number varies in a smooth manner due to ellipticity (see below). The same parity condition is mentioned in [17,18], but the in-plane-orientated PCNLC situation is different. The in-plane E- and O-modes remain orthogonal while their linearly polarized projections interfere. Therefore, the in-plane interference requires crossed polarizers. In contrast, with PCTN neither orthogonality nor polarizers are required.

The closer the mode numbers, the stronger the mode coupling with the growing overlap integral, and the more the distance of level repulsion. The series of avoided-crossing regions in Fig. 6 (regions b and d) must be extended to voltages higher than 2 V (region f), where the coupling occurs for T-mode and L-mode with the neighboring mode numbers. As a result of this strongest coupling, T-mode No. 68 jumps to the neighboring long-wave peak and L-mode No. 69 jumps to the neighboring short-wave peak. The mode number inside the transmission peak is shifted to ± 1, accordingly.

Figure 8 shows the L-mode local optical field intensity (squared electric field strength averaged in time) inside the PCTN. Nodes and antinodes of the standing wave are dumped in the middle, which follows from ellipticity of opposite running waves. In the extreme case, two opposite circularly polarized waves of the same sense of rotation interfere without nodes. Nodes of vertical polarization are compensated by antinodes of horizontal polarization, and vice versa. The illustrated oscillation suppression provides a mechanism for a mode to change its integral mode number.

VI. CONCLUSIONS

We have considered a one-dimensional PC playing the role of a resonator with a tunable TN anisotropic medium. A major experimental fact, the presence of satellite peaks, has been explained by the Mauguin condition violation and the coupling between L- and T-modes. The L-modes are coupled with T-modes without peak crossing in the case of same parity: The mode jumps to the neighboring transmission peak and changes the mode number of the peak. This one-dimensional PCTN system presents an extremely simplified example of avoided crossing, which has been well known in the multidimensional, multichannel systems [35].

Four essential ranges of applied voltages show distinct peculiar physics. No changes are observed when the applied voltage is smaller than the Fréedericksz threshold. The threshold voltage promotes a prompt spectral shift of the L-mode series to a shorter-wavelength range while the T-mode series remains at fixed wavelengths. At higher voltages the Mauguin condition is broken due to the unwinding effect, which allows coupling of T-modes with L-modes of opposite parity. After the LC twist is removed by a voltage-induced homeotropic layer, the L- and T-modes become linearly polarized and equivalent because of the spatial symmetry. The L- and T-modes of the same number combine to form doublets. These doublets shift to a homeotropic mode as the integral refractive index goes down to ordinary refractive index.

The PCTN structure suggests a sort of potential for practical application such as a light valve, monochromatic selector, etc. Besides of the mentioned spectral and electro-optical applications, the high-precision method that has been utilized in this study can also provide an alternative way for obtaining the LC elastic constants through simulation of the inverse problem.

ACKNOWLEDGMENTS

This work was supported in part by DSP Grant No. 2.1.1/3455; RAS Grants No. 3.9.1 and No. 21.1, SB RAS Grants No. 5 and No. 144, and by the National Science Council of Taiwan under Grant No. NSC 98-2923-M-033-001-MY3.

[1] J. D. Joannopoulos, S. G. Johnson, J. N. Winn, and R. D. Meade, in *Photonic Crystals: Molding the Flow of Light*, 2nd ed. (Princeton University Press, Princeton, NJ, 2008), p. 286.
[2] H. Kitzerow, Liq. Cryst. Today **11**, 3 (2002).
[3] V. F. Shabanov, S. Ya. Vetrov, and A. V. Shabanov, *Optics of Real Photonic Crystals: Liquid Crystal Defects, Irregularities* (SB RAS Publisher, Novosibirsk, 2005), in Russian.
[4] A. E. Miroshnichenko, I. Pinkevych, and Y. S. Kivshar, Opt. Express **14**, 2839 (2006).
[5] A. E. Miroshnichenko, E. Brasselet, and Y. S. Kivshar, Appl. Phys. Lett. **92**, 253306 (2008).
[6] V. A. Gunyakov, V. P. Gerasimov, S. A. Myslivets, V. G. Arkhipkin, S. Ya. Vetrov, G. N. Kamaev, A. V. Shabanov, V. Ya. Zyryanov, and V. F. Shabanov, Tech. Phys. Lett. **32**, 951 (2006).
[7] V. G. Arkhipkin, V. A. Gunyakov, S. A. Myslivets, V. Ya. Zyryanov, and V. F. Shabanov, Eur. Phys. J. E **24**, 297 (2007).
[8] V. G. Arkhipkin, V. A. Gunyakov, S. A. Myslivets, V. P. Gerasimov, V. Ya. Zyryanov, S. Ya. Vetrov, and V. F. Shabanov, J. Exp. Theor. Phys. **106**, 388 (2008).
[9] S. Ya. Vetrov and A. V. Shabanov, J. Exp. Theor. Phys. **74**, 719 (1992).
[10] Y. Shimoda, M. Ozaki, and K. Yoshino, Appl. Phys. Lett. **79**, 3627 (2001).
[11] S. Ya. Vetrov and A. V. Shabanov, J. Exp. Theor. Phys. **93**, 977 (2001).
[12] R. Ozaki, T. Matsui, M. Ozaki, and K. Yoshino, Jpn. J. Appl. Phys. **41**, L1482 (2002).
[13] J. Schmidtke, W. Stille, and H. Finkelmann, Phys. Rev. Lett. **90**, 083902 (2003); T. Matsui, M. Ozaki, and K. Yoshino, Phys. Rev. E **69**, 061715 (2004); A. V. Shabanov, S. Ya. Vetrov, and A. Yu. Karneev, J. Exp. Theor. Phys. Lett. **80**, 181 (2004).
[14] J. S. Patel and Y. Silberberg, Opt. Lett. **16**, 1049 (1991); J. S. Patel, M. A. Saifi, D. W. Berreman, Chinlon Lin, N. Andreadakis, and S. D. Lee, Appl. Phys. Lett. **57**, 1718 (1990).
[15] V. Ya. Zyryanov, V. A. Gunyakov, S. A. Myslivets, V. G. Arkhipkin, and V. F. Shabanov, Mol. Cryst. Liq. Cryst. **488**, 118 (2008).
[16] V. A. Gunyakov, S. A. Myslivets, A. M. Parshin, V. Ya. Zyryanov, V. G. Arkhipkin, and V. F. Shabanov, J. Tech. Phys. **55**, 1484 (2010).
[17] V. Ya. Zyryanov, S. A. Myslivets, V. A. Gunyakov, A. M. Parshin, V. G. Arkhipkin, V. F. Shabanov, and W. Lee, Opt. Express **18**, 1283 (2010).
[18] V. Ya. Zyryanov, V. A. Gunyakov, S. A. Myslivets, V. G. Arkhipkin, and V. F. Shabanov, Nanotechnologies in Russia **3**, 751 (2008).
[19] Y.-T. Lin, W.-Y. Chang, C.-Y. Wu, V. Ya. Zyryanov, and W. Lee, Opt. Express **18**, 26959 (2010).
[20] M. Schadt and W. Helfrich, Appl. Phys. Lett. **18**, 127 (1971).
[21] V. K. Fréedericksz and V. Zolina, Trans. Faraday Soc. **29**, 919 (1933).
[22] H. J. Deuling, Mol. Cryst. Liq. Cryst. **19**, 123 (1972).
[23] F. M. Leslie, Mol. Cryst. Liq. Cryst. **12**, 57 (1970).
[24] M. G. Tomilin, in *Interaction of Liquid Crystals with a Surface* (Politehnika, St. Petersburg, 2001), p. 326, in Russian.
[25] R. P. Fedorenko, in *Introduction in the Computing Physics: Manual for High Schools* (Intelligence Publisher, Dolgoprudny, 2008), p. 503, also see p. 80, in Russian.
[26] G. A. Korn and T. M. Korn, *Mathematical Handbook for Scientists and Engineers: Definitions, Theorems, and Formulas for Reference and Review*, 2nd ed. (McGraw-Hill, New York, 1968).
[27] S. Teitler and B. W. Henvis, J. Opt. Soc. Am. **60**, 830 (1970).
[28] D. W. Berreman, J. Opt. Soc. Am. **62**, 502 (1972).
[29] P. Yeh, J. Opt. Soc. Am. **69**, 742 (1979).
[30] S. P. Palto, J. Exp. Theor. Phys. **92**, 552 (2001).
[31] C. H. Gooch and H. A. Tarry, J. Phys. D: Appl. Phys. **8**, 1575 (1975); A. Yariv and P. Yeh, *Optical Waves in Crystals: Propagation and Control of Laser Radiation* (Wiley, Hoboken, NJ, 1984).
[32] P. Yeh, in *Optics of Liquid Crystal Displays* (John Wiley & Sons, Hoboken, NJ, 1999), p. 438.
[33] H. A. Haus, *Waves and Fields in Optoelectronics,* Prentice Hall Series in Solid-State Physical Electronics, Sec. 3.9 (Prentice-Hall, Englewood Cliffs, NJ, 1984), p. 402.
[34] J. von Neumann and E. P. Wigner, Physikal. Z. **30**, 467 (1929).
[35] Yu. N. Demkov and P. B. Kurasov, Theor. Math. Phys. **153**, 1407 (2007).